

MILCANN : A neural network assessed tSZ map for galaxy cluster detection

G. Hurier¹, N. Aghanim² & M. Douspis²

¹ Centro de Estudios de Física del Cosmos de Aragón (CEFCA), Plaza de San Juan, 1, planta 2, E-44001, Teruel, Spain

² Institut d'Astrophysique Spatiale, CNRS (UMR8617) Université Paris-Sud 11, Bâtiment 121, Orsay, France

e-mail: ghurier@cefca.es

Received / Accepted

Abstract

We present the first combination of thermal Sunyaev-Zel'dovich (tSZ) map with a multi-frequency quality assessment of the sky pixels based on Artificial Neural Networks (ANN) aiming at detecting tSZ sources from sub-millimeter observations of the sky by Planck. We construct an adapted full-sky ANN assessment on the fullsky and we present the construction of the resulting filtered and cleaned tSZ map, MILCANN. We show that this combination allows to significantly reduce the noise fluctuations and foreground residuals compared to standard tSZ maps. From the MILCANN map, we constructed the HAD tSZ source catalog that consists of 3969 sources with a purity of 90%. Finally, We compare this catalog with ancillary catalogs and show that the galaxy-cluster candidates in the HAD catalog are essentially low-mass (down to $M_{500} = 10^{14} M_{\odot}$) high-redshift (up to $z \leq 1$) galaxy cluster candidates.

Key words. Cosmology: Observations – Cosmic background radiation – Sunyaev-Zel'dovich effect

1. Introduction

Galaxy clusters are the largest virialized structures in the Universe. They are excellent tracers of the matter distribution, and their abundance can be used to constrain the cosmological model in an independent way. Galaxy clusters are objects composed of dark matter, stars, cold gas and dust in galaxies, and a hot ionized intra-cluster medium (ICM). Consequently, they can be identified in optical bands as concentrations of galaxies (see e.g. Abell et al. 1989; Gladders & Yee 2005; Koester et al. 2007; Rykoff et al. 2013), they can be observed in X-rays by the bremsstrahlung emission produced by the ionized intra-cluster medium (ICM) (see e.g. Bohringer et al. 2000; Ebeling et al. 2000, 2001; Böhringer et al. 2001). The same hot ICM also creates a distortion in the black-body spectrum of the cosmic microwave background (CMB) through the thermal Sunyaev-Zel'dovich (tSZ) effect (Sunyaev & Zeldovich 1969, 1972), an inverse-Compton scattering between the CMB photons and the ionized electrons in the ICM.

Through the tSZ effect, CMB photons receive an average energy boost by collision with hot (a few keV) ionized electrons of the intra-cluster medium (see e.g. Birkinshaw 1999; Carlstrom et al. 2002, for reviews). The thermal SZ Compton parameter in a given direction, \mathbf{n} , on the sky is given by

$$y(\mathbf{n}) = \int n_e \frac{k_B T_e}{m_e c^2} \sigma_T ds \quad (1)$$

where ds is the distance along the line-of-sight, \mathbf{n} , and n_e and T_e are the electron number density and temperature, respectively. In units of CMB temperature the contribution of the tSZ effect for a given observation frequency ν is

$$\frac{\Delta T_{\text{CMB}}}{T_{\text{CMB}}} = g(\nu) y. \quad (2)$$

Neglecting relativistic corrections we have

$$g(\nu) = \left[x \coth\left(\frac{x}{2}\right) - 4 \right], \quad (3)$$

with $x = h\nu/(k_B T_{\text{CMB}})$. At $z = 0$, where $T_{\text{CMB}}(z = 0) = 2.726 \pm 0.001$ K, the tSZ effect is negative below 217 GHz and positive for higher frequencies.

tSZ surveys provides a different window on the cluster population compared to other large scale structure tracers, allowing to detect higher redshift objects. They also provide a nearly mass-limited census of the cluster population at high redshift, where abundance is strongly sensitive to cosmological parameters (Carlstrom et al. 2002; Planck Collaboration results. XX 2014). The tSZ integrated Comptonisation parameter, Y_{SZ} , is related to the integrated electron pressure and hence the total thermal energy of the cluster gas. It correlates with mass with a low intrinsic scatter and small dependence on the dynamical properties of the cluster (eg: da Silva et al. 2004; Kay et al. 2012; Hoekstra et al. 2012; Planck Collaboration et al. 2013; Sifón et al. 2013).

Recent large catalogues based on measurements of the tSZ effect have been produced from *Planck* (Planck Collaboration early results. VIII 2011; Planck Collaboration results XXXII 2015), ACT (Marriage et al. 2011), and SPT (Bleem et al. 2014) data.

Several tSZ sources detection algorithm (see e.g., Melin et al. 2006; Carvalho et al. 2009) have been proposed and compared (Melin et al. 2012), demonstrating that a multi-frequency approach for the tSZ detection is more robust than a tSZ map-based approach. Especially, tSZ map-based detection methods present a significantly lower level of purity than multi-frequency-based approaches.

The expected number of galaxy clusters is extremely sensitive to cosmological parameters (The Dark Energy Survey Collaboration 2005; Vanderlinde et al. 2010; Sehgal et al. 2011; Böhringer et al. 2014; Planck Collaboration results. XX 2014). An important factor that limits the accuracy in the determination of cosmological parameters is the contamination of the tSZ signal by other astrophysical emissions, mainly radio, infra-red point sources, and cosmic infra-red background (Dunkley et al. 2011; Shirokoff et al. 2011; Reichardt et al. 2012; Sievers et al. 2013; Planck Collaboration results. XXI 2014) that can produce spurious galaxy cluster detections and/or a significant bias the measured tSZ fluxes. A tailored quality assessment of the tSZ signal from galaxy clusters is thus required to produced high-purity robust galaxy cluster samples detected with the tSZ effect.

An artificial neural network (ANN) based quality assessment method has been proposed (Aghanim et al. 2015) and applied to Planck galaxy cluster catalogs (Planck Collaboration 2015 results XXVII 2016). This method uses the Planck multi-frequency data to assess the quality of the tSZ signal by decomposing the measured signal into the different astrophysical components intervening at the Planck frequencies. It showed that the first Planck tSZ-source catalog (Planck Collaboration results XXXII 2015) suffers from contamination by galactic CO sources and infra-red emission (Aghanim et al. 2015). Recent follow-up (van der Burg et al. 2016) of Planck tSZ sources in the optical have shown the efficiency of this ANN-based quality assessment by confirming the spurious nature of tSZ sources with bad quality criteria.

In this work, we propose a new approach for galaxy cluster detection, that uses an ANN-based filtering of tSZ full-sky maps. First, in section 2, we present the different dataset used in this work. In section 3 we detail the construction of the ANN-based filter that enables to perform tSZ sources detection in the tSZ-map space competitively with multi-frequency approaches. Then, in section 4, we construct a sample galaxy cluster candidates and we present a detailed characterization of this new galaxy cluster detection method. Finally, in sect. 5 we perform a multi-wavelength assessment of the detected galaxy cluster candidates.

2. Data

For the present analysis we used several dataset:

- Planck intensity maps from 70 to 857 GHz (Planck Collaboration 2015 results I 2016), assuming spectral response from Planck Collaboration results IX (2014) and gaussian beams (Planck Collaboration results. VII 2014).
- Planck full-sky lensing map (Planck Collaboration et al. 2015),
- Catalogs used to describe astrophysical sources properties:
 - a meta catalog of X-ray detected galaxy cluster (MCXC, Piffaretti et al. 2011, and reference therein),
 - the WHL12 catalogue (132, 684 objects, Wen et al. 2012) of galaxy clusters detected in the SDSS data York et al. 2000,
 - a catalog of tSZ sources detected in Planck data (PSZ1 hereafter, see Planck Collaboration results XXXII 2015).
 - catalogues of sources detected at 30 GHz and 353 GHz from the Planck Catalogue of Compact Sources (PCCS) (Planck Collaboration results XXVIII 2014)

- Ancillary data used to characterize galaxy cluster candidates:
 - the reprocessed IRAS maps, IRIS (Improved Reprocessing of the IRAS Survey, Miville-Deschênes & Lagache 2005),
 - The AllWISE Source Catalog¹

3. Artificial neural network filtering

In this section, we describe how we build an artificial neural network (ANN) filtered tSZ map. ANN-based quality assessment enables to directly learn from the data the characteristic signature of real tSZ sources and spurious signal using a reference sample of astrophysical sources. This approach has been shown as an efficient method to identify spurious tSZ detections (Aghanim et al. 2015; van der Burg et al. 2016) from Planck tSZ candidate catalogs (Planck Collaboration results XXXII 2015; Planck Collaboration 2015 results XXVII 2016). In the following, we extend this approach to each pixel of the sky-maps rather than to a pre-selected sample of tSZ candidates.

3.1. Neural Network Training

We summarize here the key elements of the ANN training process and refer to Aghanim et al. (2015) for a more detailed description.

3.1.1. SED fitting

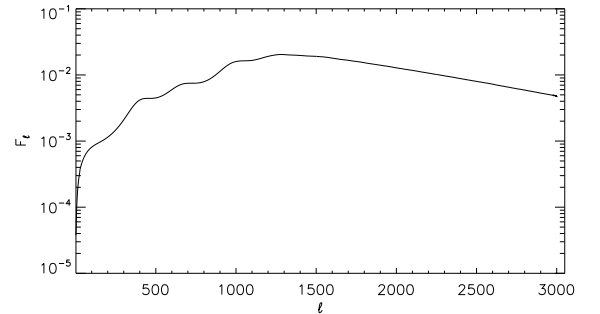


Figure 1. Matched filter in ℓ space used for the ANN-based quality assessment.

Following Aghanim et al. (2015), we focus on the astrophysical emissions that affect the most the tSZ detection in multifrequency experiments. This issue was addressed in both Planck Collaboration et al. (2011) and Planck Collaboration results XXXII (2015). We model the spectral energy distribution (SED) taking into account five components: the thermal SZ (tSZ) effect neglecting relativistic corrections; the CMB signal; and the CO emission. We also add an effective IR component representing the contamination by dust emission, cold Galactic sources, and CIB fluctuations; and an effective radio component accounting for diffuse radio and synchrotron emission and radio sources. The flux in each channel, i.e. frequency, is then written as

$$F_\nu = A_{\text{SZ}} F_{\text{SZ}}(\nu) + A_{\text{CMB}} F_{\text{CMB}}(\nu) + A_{\text{IR}} F_{\text{IR}}(\nu) + A_{\text{RAD}} F_{\text{RAD}}(\nu) + A_{\text{CO}} F_{\text{CO}}(\nu) + N(\nu), \quad (4)$$

¹ <http://wise2.ipac.caltech.edu/docs/release/allwise/expsup/>

where $F_{\text{SZ}}(\nu)$, $F_{\text{CMB}}(\nu)$, $F_{\text{IR}}(\nu)$, $F_{\text{RAD}}(\nu)$, and $F_{\text{CO}}(\nu)$ are the spectra of tSZ, CMB, IR, radio, and CO emissions; A_{SZ} , A_{CMB} , A_{IR} , A_{RAD} , and A_{CO} are the corresponding amplitudes; and $N(\nu)$ is the instrumental noise.

For $F_{\text{IR}}(\nu)$, we consider a modified black-body spectrum with temperature $T_d = 17$ K and index $\beta_d = 1.6$. This assumption is representative of the dust properties at high galactic latitudes. The contribution from CIB fluctuations affects the flux measurement, but is not a major contamination from the point of view of the detection, i.e. spurious sources. For $F_{\text{RAD}}(\nu)$, we consider a power law emission, ν^{α_r} , with index $\alpha_r = -0.7$ in intensity units representative of the average property of the radio emission. In order to compute the SED of the considered pixels, we use the Planck frequency maps from 70 to 857 GHz. First, each map is set to a resolution of 13 arcmin, i.e. the lowest resolution (70 GHz map).

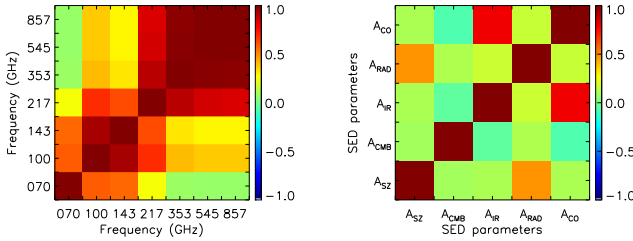


Figure 2. Left panel: correlation matrix of the measured fluxes from 30 to 857 GHz estimated on 2000 random positions over the sky. Right panel: correlation matrix of fitted SED parameters from the same positions.

By contrast to Aghanim et al. (2015), we compute the flux for each pixel and each frequency using a match-filter in ℓ space presented in Fig. 1. We choose this approach, rather than the aperture photometry to improve the photometry of tSZ sources. To build this filter, we assume the power spectrum, y_ℓ , of a tSZ signal from a cluster with $R_{500} = 5'$ (point-like with respect to the Planck experiment), and a universal pressure profile (Arnaud et al. 2010). We also consider the power spectrum of the CMB, C_ℓ^{CMB} , computed using Planck best-fit cosmology (Planck Collaboration 2015 results XIII 2015), and the power spectrum of the noise, C_ℓ^{NN} , in the 100 GHz channel (estimated using half-ring map difference) which is the frequency channel with the highest noise level. We note that to obtain model independent flux estimations, the match-filter has to be the same at all frequency. Considering that for relevant frequency channels for the tSZ flux estimation (100 to 217 GHz), angular scales ($\ell \in [1000, 2000]$), and galactic latitudes the thermal dust amplitude from the Milky Way is small compared to the CMB contribution, we do not include a galactic thermal dust contribution in the computation of the match filter. Then the filter is computed as

$$F_\ell = \sqrt{\frac{y_\ell}{C_\ell^{\text{CMB}} + C_\ell^{\text{NN}}}}, \quad (5)$$

and applied on the harmonic space coefficients, $a_{\ell,m} = F_\ell a_{\ell,m}$, of Planck intensity maps from 70 to 857 GHz. We verified that our results do not significantly depends on the chosen amplitude of C_ℓ^{NN} for the match-filter computation.

Thus we derive an SED, F_ν , for each pixels, which is fitted assuming the model in Eq. 4, where we fit for A_{SZ} , A_{CMB} , A_{IR} , A_{RAD} , and A_{CO} through a linear fit of the form

$$\mathbf{A} = (\mathcal{F}^T C_N^{-1} \mathcal{F})^{-1} \mathcal{F}^T C_N^{-1} F_\nu, \quad (6)$$

with the mixing matrix \mathcal{F}^T , the instrumental noise covariance matrix C_N , and \mathbf{A} a vector containing the fitted parameters. In this approach, C_N only accounts for the instrumental noise, and we implicitly assume that the five components considered in the model reproduce the astrophysical signal in the data.

The efficiency of the dimensionality reduction² is illustrated in Fig. 2 (right panel), where we show the correlation matrix of the fitted SED parameters, compared to the correlation matrix of measured fluxes from 70 to 857 GHz (left panel). We observe that we have a high degree of correlation between frequencies, especially at low frequency due to the CMB component (< 217 GHz), and at higher frequency (> 217 GHz) due to the thermal component. In contrast, in the SED parameter space, we observe that the correlation matrix is almost diagonal, except for a spatial correlation between thermal dust and CO emission. This correlation is the consequence of the thermal dust emission from molecular clouds, and is thus physically motivated. We also note a significant correlation between the tSZ effect and the radio emission. This correlation is produced by the similarities of tSZ and radio SEDs in Planck low-frequency channels that dominates the tSZ flux estimation. Indeed, the tSZ effect is negative at low-frequency and consequently in terms of best-fit a high tSZ flux can be compensated by a strong radio emission, which induces a high degree of correlation between tSZ and radio emission fluxes.

We also observe that the match-filtering approach for the SED estimation enables to obtain a correlation matrix for SED parameters which is more diagonal, especially for the tSZ amplitude A_{SZ} , than an aperture photometry SED estimate (see Fig. 2 in Aghanim et al. 2015, for comparison).

3.1.2. Full-sky ANN-based quality assessment

We consider a standard three-layer back-propagation ANN to separate pixels of the sky maps into three populations of reliable quality (the *Good*), unreliable quality/false (the *Bad*), and noisy sources (the *Ugly*). The inputs of the neural network consist of the five SED parameters and the outputs represent the three classes used to classify each sky pixel.

We briefly present here the basics of the artificial neural network method. We define

$$Q = g(\mathcal{W}_o g(\mathcal{W}_h (\mathcal{W}_r F_\nu + \mathbf{b}_r) + \mathbf{b}_h) + \mathbf{b}_o), \quad (7)$$

where $g(x) = 1/(1 + \exp(-x))$ is the activation function, $\mathcal{W}_r = (\mathcal{F}^T C_N^{-1} \mathcal{F})^{-1} \mathcal{F}^T C_N^{-1}$ corresponds to a physically-based dimensional reduction, \mathcal{W}_h are the weights between input and hidden layers, \mathcal{W}_o are the weights between hidden and output layers, \mathbf{b}_h are the biases between input and hidden layers, and \mathbf{b}_o are the biases between hidden and output layers.

To train the neural network, we use the same sample for *Good*, *Bad*, and *Ugly* classes as in Aghanim et al. (2015). We

² The projection of the measured SED on a basis of physically motivated SEDs allows to reduce the number of parameters that describe the measured SED. This method can be compared to principal component analysis, using a model-based basis instead of eigenvector of the observations.

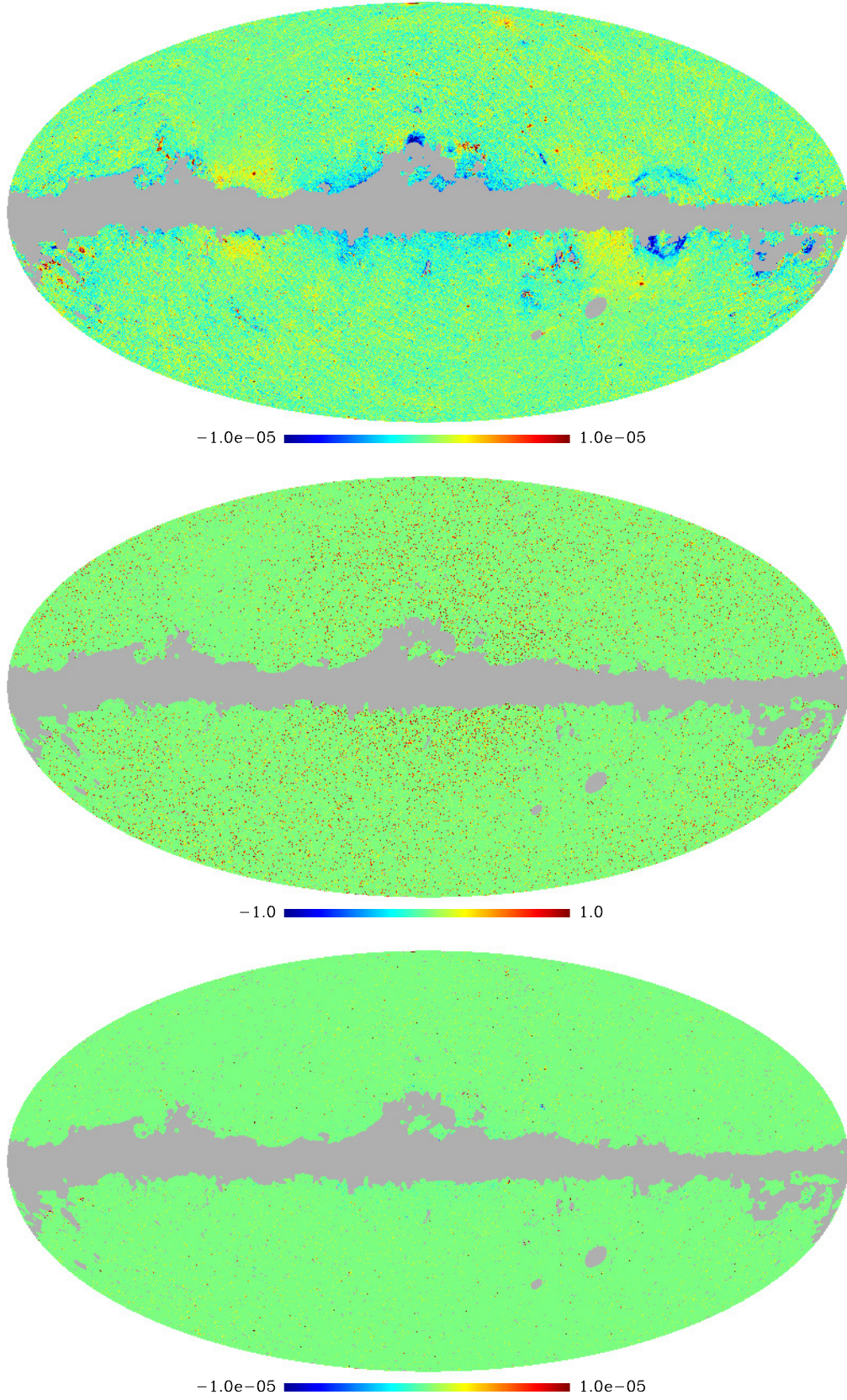


Figure 3. From top to bottom: Planck tSZ MILCA map, neural network filter, MILCANN map, for the full-sky in mollweide projection. Grey regions are masked due to galactic foregrounds or point sources contamination.

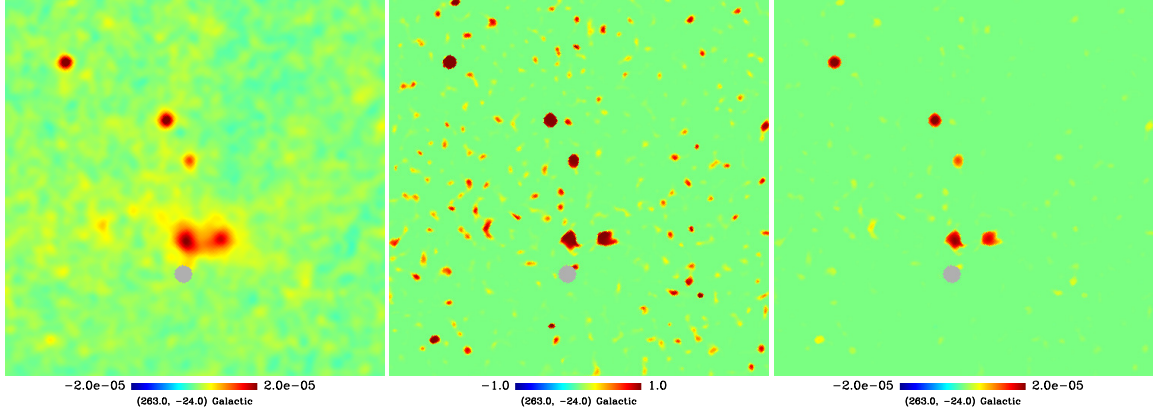


Figure 4. From left to right: Planck tSZ MILCA map, neural network filter, MILCANN map, for a patch of 8.5×8.5 degrees in gnomonic projection centered on galactic coordinates $(l, b) = (263^\circ, -24^\circ)$. Grey regions are masked due to point sources contamination.

adapt the the ANN to the match-filter SED estimation. Thus, we use the value in the central pixel toward each source as a proxy of the flux of the considered source. We split the training sample into two sub-samples, the first one used to train the ANN, and the second one used to prevent over-training of the ANN.

We defined the error on the classification as

$$E = \frac{1}{2} \sum_{\text{class}} (Q_{\text{class}}^{(\text{true})} - Q_{\text{class}})^2, \quad (8)$$

where class stands for *Good*, *Bad*, or *Ugly* and $Q_{\text{class}}^{(\text{true})} = 1$ or 0 depending on whether the source belongs to the considered class.

3.2. tSZ quality assessed map

3.2.1. MILCA Planck tSZ map

We perform the construction of a tSZ map with the MILCA method (Hurier et al. 2013), using Planck HFI from at 100 to 857 GHz. We verified that including frequencies from 30 to 70 GHz does not change significantly the reconstructed map, especially at galaxy cluster scales.

We performed the construction of the tSZ map using 8 filters in spherical harmonic space. For the first three filters we used 2 constraints (tSZ and CMB), and for the last five filters we only used a constraint on the tSZ SED. The map reconstruction is performed with an effective FWHM of 7 arcmin. For all filters, 2 degrees of freedom have been used to minimize the variance of the noise (see Hurier et al. 2013, for a detailed description of the MILCA method).

In Fig. 3, we show the MILCA full-sky map at 7 arcmin FWHM. Figure 4 shows a zoom on a small region of 8.5×8.5 degrees where bright galaxy clusterS can be observed. In the full-sky map, we observe a significant amount of foreground residuals near the galactic plane, where synchrotron and free-free residuals appear as negative biases in the tSZ y-map signal. We also observe contamination by bright galactic cirrus correlated with the zodiacal light. As demonstrated in previous works (Hurier et al. 2013; Planck Collaboration 2015 results XXII 2015), the main sources of contamination in tSZ maps built from Planck intensity maps are radio point sources, CO, and CIB

emission. Radio point sources produce a negative signal in terms of Compton parameter, thus they can be easily separated from a real tSZ-structure (Hurier et al. 2013). Significant CO emission is essentially located at low galactic latitudes, and can be masked for galaxy clusters detection purposes. CIB emission is more complex to deal with, as it is homogeneously distributed over the sky. In Sect. 3.2.3, we will propagate CIB-induced uncertainties.

3.2.2. MILCANN map

On Fig. 3, we observed that the tSZ map reconstructed from Planck data suffers from bias due to residulas from other astrophysical emission. Using the neural-network based quality assessment presented in sect. 3.1.2, we can obtain an estimation of the quality of the tSZ signal in each line-of-sight of the sky. First, we define an ANN-based filter, Q_N , as

$$Q_N = Q_{\text{GOOD}}(1 - Q_{\text{BAD}}), \quad (9)$$

Where Q_{GOOD} and Q_{BAD} are the ANN classification output values for the *Good* and *Bad* classes. By construction this ANN-filter ranges from 0 to 1, with values close to 1 for pixels that present a high-quality tSZ signal. We did not apply any weighting over the *Ugly* ANN output to avoid a catastrophic reduction of low signal to noise ratio galaxy clusters. The noise amplitude reduction is already performed by the weighting over Q_{GOOD} .

In Fig. 3 and 4, we show the full-sky ANN filter described in Sect. 3.1.2 and the MILCANN map. We observe a clear spatial correlation between the ANN filter and the tSZ MILCA map. However, we observe that the ANN filter presents values close to 1 even for some pixels where no clear tSZ excess can be observed. These misclassified pixels are produced by chance alignment between noise structure and tSZ spectral signature. As a consequence, a tSZ sources detection performed directly on the ANN filter map would leads to low-purity samples.

Then, we convolve the MILCA tSZ map, noted \hat{y} , by the matched filter used for the SED fitting in section 3.1.1. Thus, the filtered MILCA map, \hat{y}_f , has a transfert function consistent with the map used to perform the ANN classification.

Finally, we derived the MILCANN map as

$$M_{\text{MILCANN}} = \hat{y}_f Q_N. \quad (10)$$

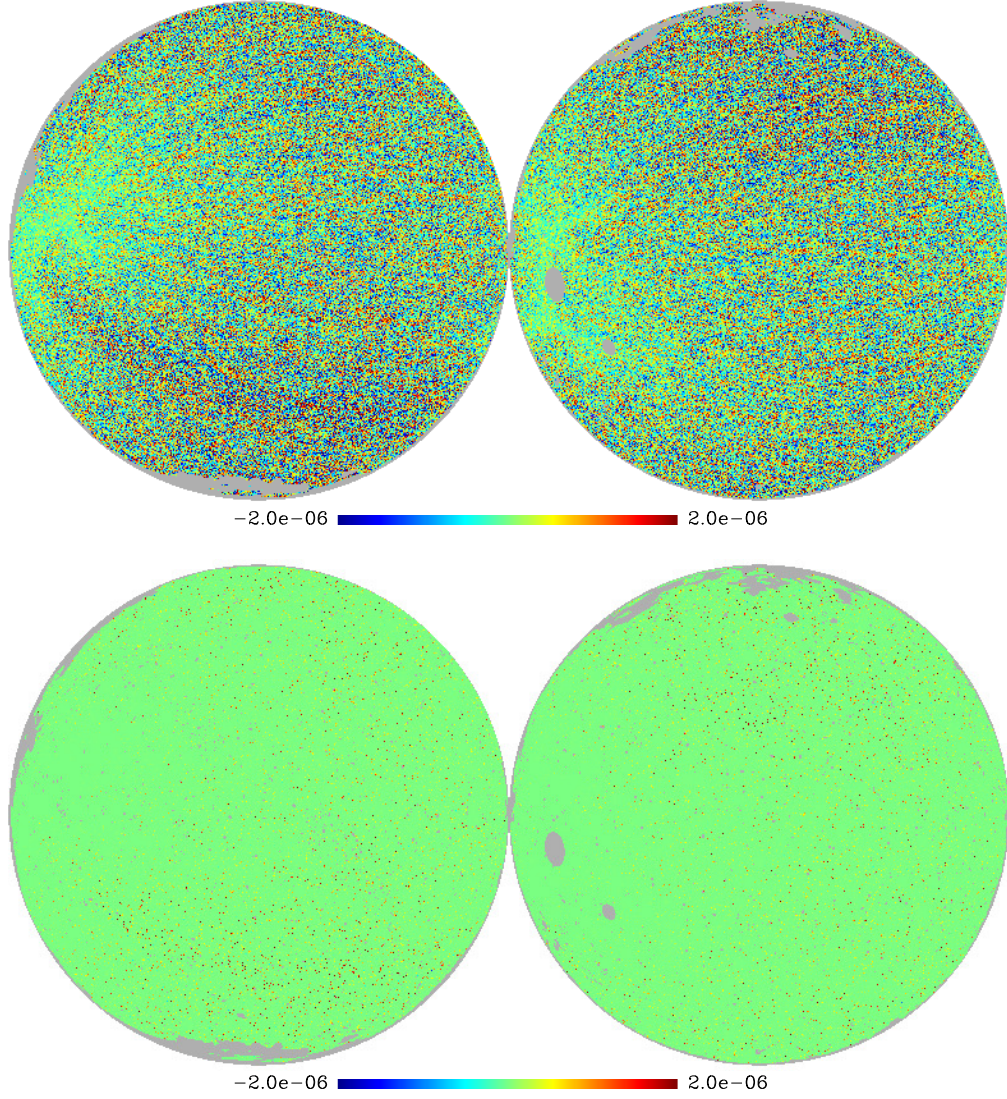


Figure 5. From top to bottom: Planck tSZ MILCA noise map MILCANN noise map for the full-sky in orthographic projection. Grey regions are masked due to point-source contamination.

On Fig. 3, the MILCANN map shows that the ANN-filter has significantly removed the foreground contamination, especially near the galactic plane, where synchrotron and free-free contamination have been completely suppressed. Similarly, the contamination produced by high latitude galactic cirrus has been filtered out by the ANN. On Fig. 4, we also observe that the MILCANN map presents a significantly reduced background, but almost conserves the intensity of bright tSZ pixels. However, we stress that the ANN filtering does not conserve the shape of the tSZ sources, as it will modify the intensity of faint tSZ pixels in the outskirts of galaxy clusters.

As shown by Melin et al. (2012), tSZ-map based galaxy cluster detection methods suffer from a high level of contamination by spurious detection since it is a priori not possible to disentangle real tSZ emission from biases induced by other astrophysical emission residuals. By contrast and due to its significant reduced residual signals, the MILCANN map seems well suited for

galaxy cluster detection. However, it cannot be used to produced accurate estimation of the flux or the shape of tSZ sources.

3.2.3. Noise and CIB-residuals simulations

We have shown qualitatively that MILCANN tSZ map presents a significantly reduced background compared to MILCA tSZ map. In this section, we describe our modeling of the noise and CIB-residuals in the MILCA and MILCANN tSZ maps to quantify the improvement obtained by applying an ANN filtering.

The tSZ maps are derived from component separation methods. They are constructed through the linear combination of Planck frequency maps that depends on the angular scale and

the pixel, p , as

$$\hat{y} = \sum_{i,j,\nu} w_{i,p,\nu} T_{i,p}(\nu), \quad (11)$$

$T_{i,p}(\nu)$ is the *Planck* map at frequency ν for the angular filter i , and $w_{i,p,\nu}$ are the weights of the linear combination. Then, the CIB contamination in the y -map reads,

$$y_{\text{CIB}} = \sum_{i,j,\nu} w_{i,p}(\nu) T_{i,p}^{\text{CIB}}(\nu), \quad (12)$$

where $T^{\text{CIB}}(\nu)$ is the CIB emission at frequency ν . Using the weights $w_{i,p,\nu}$, and considering the CIB luminosity function, it is possible to predict the expected CIB leakage as a function of the redshift of the source by propagating the SED through the weights that are used to build the tSZ map. As shown by [Planck Collaboration 2015 results XXIII \(2015\)](#), the CIB at low- z leaks with a small amplitude in the tSZ map, whereas high- z CIB produces a higher, dominant, level of leakage. Indeed, internal-linear-combination-based component separation methods focus on Galactic thermal dust removal, and thus are less efficient to subtract high- z CIB sources that present a different SED.

The CIB power spectra have been constrained by previous *Planck* analyses (see e.g., [Planck Collaboration results XXX 2014](#)). They can be used to predict the expected CIB leakage, y_{CIB} , in the tSZ map, y .

We performed 200 Monte-Carlo simulations of CIB that follow CIB power spectra. Then, we add instrumental noise to the simulated CIB maps. Finally, we apply the weights used to build the tSZ map to these simulations. We obtained 200 realizations of instrumental noise and CIB at the *Planck* frequency maps level, consistent with noise and CIB realizations at the MILCA tSZ map level.

It is important to stress that the noise in MILCA tSZ map is by construction correlated to the noise in frequency maps. Thus, the noise on the ANN classes is also correlated with the noise in MILCA tSZ map. Consequently, if we want to produce a fair description of the noise, we have to train another neural network on the simulated maps to reproduce the correlation feature between the noise in MILCA map and the noise on ANN classification. Considering that the training of an ANN is a non-linear process, we also added CMB, point sources, and thermal dust to the noise+CIB simulations during the training process.

Finally, we build and applied the noise-based ANN to the MILCA noise+CIB-residuals simulation. On Fig. 5, we present a noise+CIB-residuals simulation before and after applying the noise-based ANN-filter, we observe that the ANN filtering allows to significantly reduce the noise level in the MILCA simulated map. From the MILCANN simulated map, we derive the standard deviation of the noise in MILCANN map by computing the local standard deviation of MILCANN simulated noise map inside a two-degree gaussian beam.

In Fig. 6, we compare the intensity distributions in MILCA and MILCANN map. For the MILCA map, we observe a significant tail of negative intensity (mainly produce by radio-sources contamination). We do not observe this contamination in the MILCANN map, as the ANN filter significantly reduces radio sources contamination. We also observe that the noise in the MILCANN map is lower than in the MILCA map by a factor of five. However, we note that the intensity of the brightest pixels in the map is not affected by the ANN filter.

We note that the noise in MILCANN is not Gaussian. Considering the correlation between the ANN filter and the noise in MILCA map, the noise in the MILCANN map does

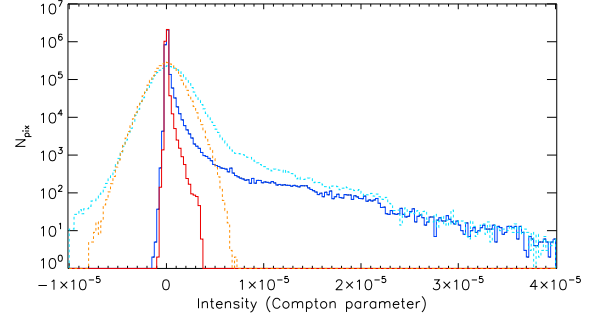


Figure 6. Intensity distribution of pixels in the tSZ maps for: the MILCA map (light blue), the MILCANN map (dark blue), simulation of noise + CIB in the MILCA map (orange), simulation of noise+CIB in the MILCANN map (red).

not present symmetric distribution. So, we are dealing with a non-Gaussian, inhomogeneous, correlated noise with an asymmetric distribution. As observed on Fig. 6, the noise is more likely to produce positive value in MILCANN map than negative value. It implies that the noise has a non-zero expectation value. Consequently, in the following we used and propagated the complete noise distribution.

3.2.4. Noise inhomogeneities

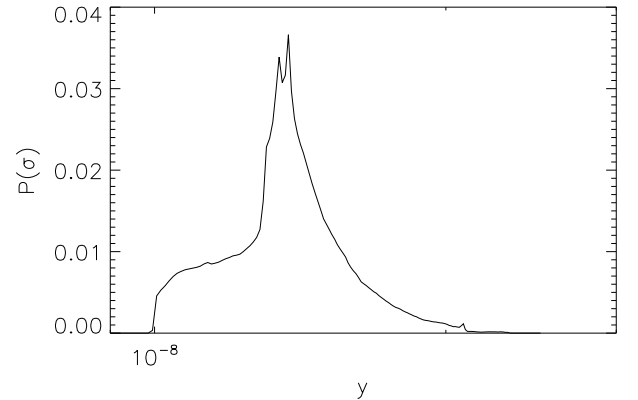


Figure 7. Distribution of the noise standard deviation, σ_y across the MILCANN full-sky map.

Due to *Planck* scanning strategy, the noise level on the sky is inhomogeneous. Ecliptic poles present a better redundancy of observations and thus a significantly lower level of noise ([Planck Collaboration 2015 results I 2016](#)).

By construction, the noise of the ANN-filter is related to the noise in MILCA map. The MILCANN map is obtained by the product of the filtered MILCA map and the ANN filter, thus the noise inhomogeneities are amplified. The distribution of the pixel-dependent noise level is presented on Fig. 7, that presents the noise standard deviation, σ_y , distribution. This quantity is estimated locally in a 4 degrees gaussian beam. The low noise regions correspond to ecliptic poles and high noise regions correspond to the ecliptic plane. To obtain a map of the signal-to-

noise ratio, we constructed the noise normalized quantity, \widehat{y}_σ , as

$$\widehat{y}_\sigma = \frac{\widehat{y}_f}{\sigma_y}. \quad (13)$$

We note that using a homogeneous threshold on \widehat{y}_σ is equivalent to using a pixel-dependent threshold on \widehat{y}_f .

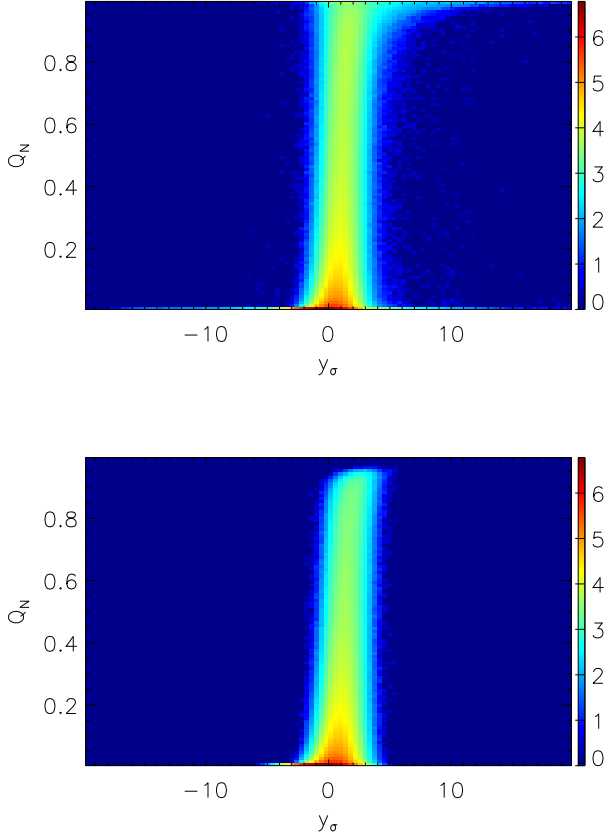


Figure 8. Distribution of the MILCANN map (top panel) and MILCANN noise simulation (bottom panel) as function of Q_N and normalized intensity, y_σ . The colors show the number of pixels in logarithmic scale.

Figure 8 presents the distributions of MILCANN map and MILCANN noise simulation respectively as a function of y_σ and Q_N . We observe that the MILCANN noise simulation does not show high- Q_N and high- y_σ pixels. We also observe that for $Q_N \simeq 0$ the MILCANN map presents a significantly larger distribution of y_σ than the noise simulation. This is produced by foreground residuals that are present in the MILCA tSZ map. We verified that these residuals are strongly correlated with the galactic latitude, which ensures that they are related to systematic effects. However, we do not observe a similar behavior at larger values of Q_N . This confirms that foreground residuals are strongly reduced using the ANN-filtering procedure, as already observed on Fig. 6.

3.2.5. ANN response

In this section, we quantify the transfert function of the ANN-filtering procedure between the tSZ intensity in the MILCA map and the tSZ intensity in the MILCANN map.

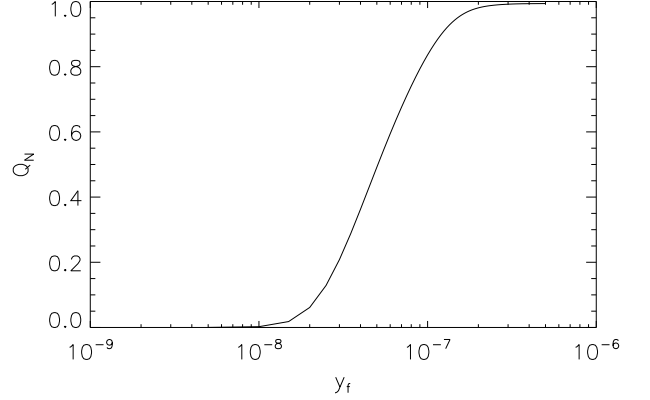


Figure 9. ANN-filter average value as a function of the match-filtered intensity.

By applying the artificial neural network filter, we reduce the noise level. To a lesser extent, we also reduce the intensity of tSZ effect from galaxy clusters. Indeed, the value of Q_N is not exactly 1 for all galaxy clusters. Additionally, the value of Q_N is sensitive to the flux of the cluster, a high flux galaxy cluster will have $Q_N \simeq 1$, whereas low flux galaxy clusters will be classified as noise and will have $Q_N \ll 1$.

Thus, we select 10 000 random pixels within the 84% mask used for the detection and we added a constant amount of an emission following a tSZ SED. This approach allows to properly account for real sky background and noise level. Then, we apply the ANN on these 10 000 modified pixels, and derived the average value for Q_N as a function of the inputted tSZ intensity, which gives the transfert function of the ANN filtering procedure.

On Fig. 9, we show the average value of the ANN-filter as a function of the filtered tSZ signal intensity, y_f . We observe that ANN response present a steep transition, all signal below $y_f = 10^{-8}$ is completely suppressed by the ANN, whereas signal above $y_f = 2 \cdot 10^{-7}$ is almost not affected by the ANN filtering. We stress that these intensities are obtained after filtering and are not consequently comparable with total tSZ intensity in MILCA map. We verified that we derive a consistent transfert function for Q_N when computed from noise simulations from Sect. 3.2.3.

4. tSZ candidate detection

In this section, we used the improved tSZ map obtained after applying the ANN-based filter to perform galaxy cluster detection. We also characterize the purity and completeness of the derived galaxy cluster candidate sample to assess the improvement compared to previous galaxy cluster catalog derived from the Planck data.

4.1. Methodology

To detect sources in MILCANN full-sky map, we applied a mask of the galactic plane and point sources detected by Planck

keeping 84% of the sky defined in [Planck Collaboration results XXXII \(2015\)](#). Then, using the noise standard deviation map computed in section 3.2.3, we homogenized the MILCANN map noise level to perform the detection in signal-to-noise unit on the full-sky with a homogeneous threshold. We applied a threshold, $y_\sigma > 3$, to the MILCANN map, and consider as detected sources all setS of adjacent pixels that are above the threshold. We finally clean multiple detections of a same object by merging detected sources in a radius of 10 arcmin (consistent with Planck angular resolution) and remove all sources detected on less than 5 pixels of 1.7×1.7 arcmin² (to avoid detections produced by anomalous pixels). We derive a sample 3969 galaxy cluster candidates. In the following, we refer to this sample of galaxy cluster candidates as the HAD catalog.

4.2. Characterization of the MILCANN detection method

In this section we characterize the detection method. We present in detail each step that allow us to compute the selection function of the galaxy cluster detection. Thus, we present a detailed description of the galaxy cluster signal transfert function across our processing.

4.2.1. Fourier space filtering response

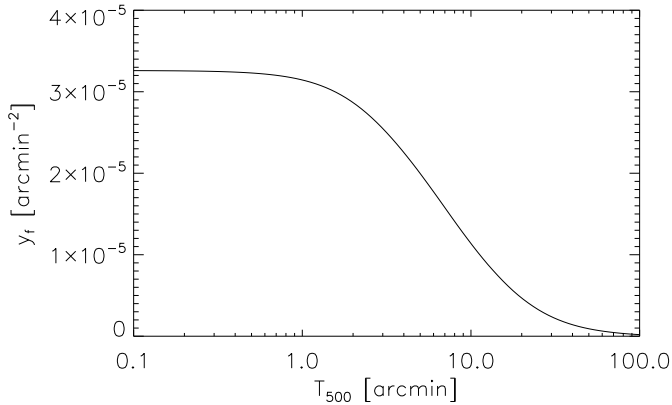


Figure 10. Central intensity of the SZ signal for a galaxy cluster with $Y_{500} = 1$ arcmin² as a function of galaxy cluster typical radius T_{500} .

Before applying the ANN-filter to build the MILCANN map, we have filtered the MILCA map using the match filter presented on Fig. 1. In this section, we present the estimation of the transfert function of this filtering process. First, we build a mock map of a sky projected tSZ signal from a galaxy cluster with $Y_{500} = 1$ arcmin² assuming a GNFW pressure profile ([Arnaud et al. 2010](#)) with 1000 pixels per R_{500} . Then, we convolve the tSZ mock map by the instrumental beam and the match filter presented in Sect. 3.1.1. We perform this procedure for values of R_{500} ranging from 0.1 to 100 arcmin. Finally, we extract the tSZ intensity at the center of the galaxy cluster on the convolved mock map.

On Fig. 10, we present the tSZ intensity, y_f , to flux ratio after applying the match-filter for a galaxy cluster with a universal pressure profile. The match-filter we use selects compact object and thus presents a response that will significantly reduce the flux

of extended galaxy clusters. However, this is not an important limitation since our main goal is to detect compact tSZ sources associated with new galaxy clusters that are either low-mass or high- z . Considering the resolution of Planck tSZ maps (roughly 7 arcmin) such galaxy clusters are point-like. Furthermore for these clusters or for more extended ones, we can compute their tSZ signal directly from the MILCA map or from the frequency maps.

4.2.2. Completeness

Applying all the steps we detailed in this section, we can write the complete processing we apply to the astrophysical signal as

$$y_\sigma = Y_{500} \frac{y_f(T_{500})Q_N(y_f)}{\sigma_y} + N_\sigma, \quad (14)$$

where Y_{500} is the tSZ flux of the galaxy cluster, y_f is the galaxy clusters match-filtered intensity presented on Fig. 10, the dependancy of Q_N with y_f is presented on Fig. 9, the distribution of the noise across the map, σ_y , is shown on Fig. 7, and N_σ is the homogenized noise in the MILCANN map.

Consequently, for a given total mass, M_{500} , and a given redshift,

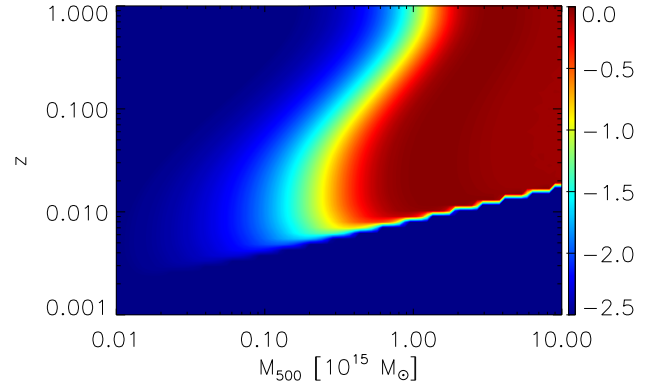


Figure 11. Completeness of the HAD catalog as a function of M_{500} and z . The color scale is logarithmic and ranges from $10^{-2.5}$ (dark blue) to 1 (red).

z , the galaxy cluster signal distribution for y_σ maps is obtained by the convolution of the $M_{500} - Y_{500}$ relation scatter (assuming scaling relation from [Planck Collaboration results. XX 2014](#), and $(1-b) = 0.8$), the distribution of σ_y , and the distribution of the noise N_σ . We assumed that the relation $M_{500} - T_{500}$ does not present any scatter.

The completeness, $C(y_\sigma)$, is then obtained as the ratio of the integral of y_σ distribution, $\mathcal{P}(y_\sigma)$, above the detection threshold normalized by the integral of the full distribution,

$$C(y_\sigma) = \frac{1}{\int_0^\infty \mathcal{P}(y_\sigma) dy_\sigma} \int_t^\infty \mathcal{P}(y_\sigma) dy_\sigma, \quad (15)$$

where t is the detection threshold applied on the y_σ map.

Figure 11 shows the completeness as a function of the mass, M_{500} and redshift, z , of a given cluster. We observe that we can detect, with a very basic detection methods applied on an optimally filtered and cleaned tSZ map, galaxy clusters down to a

typical mass of $M_{500} = 1 \cdot 10^{14} M_{\odot}$. We also observe that for very large mass ($> 2 \cdot 10^{15} M_{\odot}$) the completeness is slightly smaller than 1. This effect is produced by the match-filter that significantly reduces the tSZ effect produced by extended (massive) sources.

4.2.3. Purity

Then, we estimate the purity of the catalog by performing the detection of tSZ sources on the MILCANN map and the MILCANN noise simulation from Sect. 3.2.3. This estimate does not account for all foreground residuals in the MILCANN map. Thus this estimate may slightly over-estimate the purity of the HAD catalog. We found $N_{\text{det}}^{(1)}$ detections for the MILCANN map and $N_{\text{det}}^{(2)}$ for the simulated noise map. We performed the detection for several detection thresholds. The purity is obtained as $P = \frac{N_{\text{det}}^{(1)} - N_{\text{det}}^{(2)}}{N_{\text{det}}^{(1)}}$. On Fig. 12 we present the purity as a function of

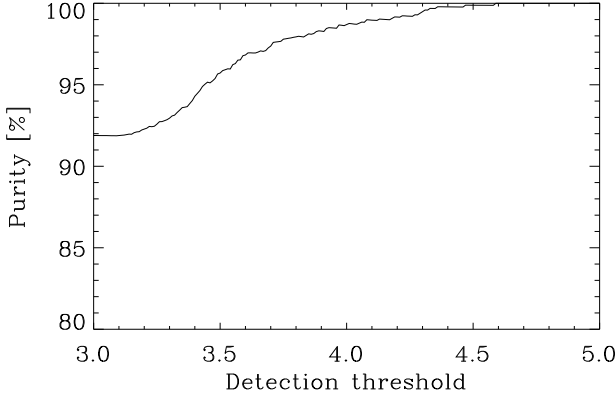


Figure 12. Purity of the HAD catalog as a function of the detection threshold.

the detection threshold. For the threshold used in the construction of the HAD catalog we derived an estimated purity above 90%.

4.3. Comparison with reference galaxy cluster catalogs

In this section, we present a brief comparison of the HAD galaxy-cluster candidate catalog and other reference catalogs. We used two approaches for the comparison.

First we compare the numbers of galaxy cluster candidates in the HAD catalog, and the predicted number of detections assuming Planck-SZ cosmology (Planck Collaboration results, XX 2014) and considering the completeness and purity of the HAD catalog. This predicted number is found to be 4082 ± 700 . The 3969 detected candidates in the HAD catalog is thus very well consistent with 4082 predicted detections from galaxy cluster based cosmological parameters.

Second, we perform a cross-match with reference galaxy cluster catalogs. We compare our detected catalog of candidates with the PSZ2 catalog. The distribution of nearest neighbors distance is shown on Fig. 13. From our 3969 detections, we find 1243 in common with the PSZ2 (and there is 418 objects in

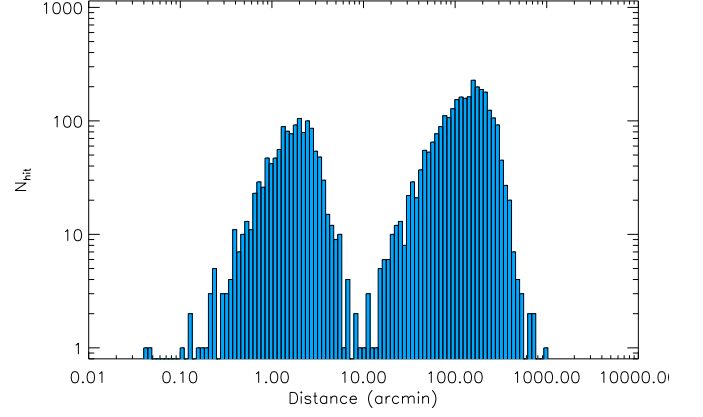


Figure 13. Nearest neighbor distance distribution between HAD sources and PSZ2 public catalog sources.

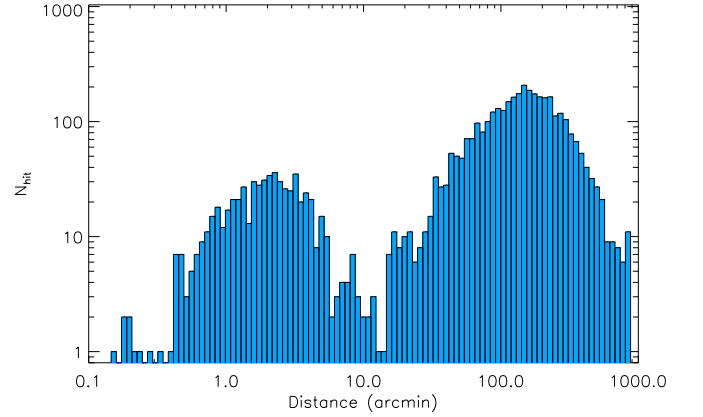


Figure 14. Nearest neighbor distance distribution between HAD sources and MCXC sources.

the PSZ2 that have no counterpart in the HAD catalog) among which 997 are confirmed galaxy clusters and have $Q_{\text{Neural}} > 0.6$ ³ in the PSZ2 catalog. We also detect 496 known clusters that are missing from PSZ2 (considering ACT, SPT, Redmapper, Wen+12, and MCXC catalogs). Figure 13 shows clearly the two populations of sources common and not common with PSZ2. For common sources we obtain a typical position mismatch below 4 arcmin compared to the position presented in the PSZ2. For very extended sources the position mismatch can reach up to 10 arcmin. This position mismatch is consistent with the Planck experiment resolution. The case of extended objects strongly depends on the exact methodology used to define the galaxy cluster position. Nevertheless, considering the number density in Planck SZ catalog and HAD catalog, within a radius of 10 arcmin the number of chance association is 15 ($\approx 1\%$ of the PSZ2 sample) and within a radius of 4 arcmin this number is 4. It implies that a 10 arcmin matching distance provides a robust association between objects.

Figure 14 presents the nearest neighbors distance distribution between HAD and MCXC objects, that presents similar properties

³ This quantity is derived from a previous quality assessment using the ANN presented in Aghanim et al. (2015).

than the matching of HAD and PSZ2 objects. The matching procedure of the HAD catalog outputs the following positional associations with reference catalogs:

- 1243 HAD sources in common with PSZ2
- 601 HAD sources matched with known X-ray clusters from MCXC (including 92 objects not in PSZ2)
- 687 HAD sources matched with over-density of galaxies ($N_{200} > 25$) from Wen+12 (including 276 objects not in PSZ2), we estimated a maximum number of chance association of 20 at 99% confidence level.
- 469 HAD sources matched with over-density of galaxies ($\Lambda > 50$) from RedMapper (including 179 objects not in PSZ2)
- 10 HAD sources matched with SPT only known clusters
- 7 HAD sources matched with ACT only known clusters

We used the redmapper red-sequence based redshifts to compute the redshift and richness, Λ , distributions of the matching population between HAD and redmapper catalogs in two cases: (i) considering all galaxy cluster candidates in the HAD catalog that match redmapper sources and (ii) candidates in the HAD catalog not contained in PSZ2 catalog that match redmapper sources.

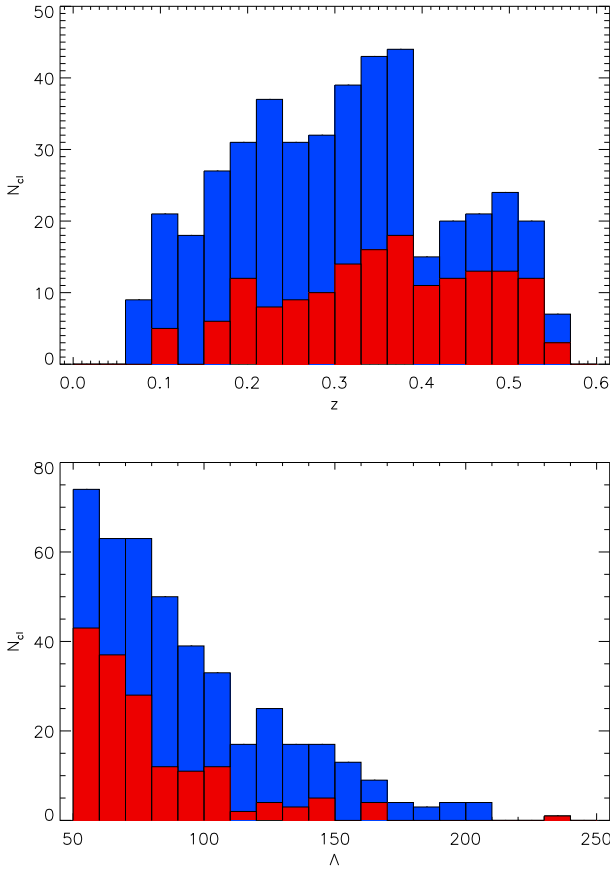


Figure 15. Top panel: redshift distribution for HAD candidates matching redmapper overdensities of galaxies (dark blue) and for HAD candidates not contained in PSZ2 catalog (red). Bottom panel: richness, Λ , distribution for HAD candidates matching redmapper overdensities of galaxies (dark blue) and for HAD candidates not contained in PSZ2 catalog (red)

On Fig. 15, we present the obtained redshift distribution for sources contained in both HAD and redmapper catalogs. We observe that new tSZ detections in the HAD catalog (not contained in the PSZ2 catalog) are essentially at higher redshift than PSZ2 galaxy clusters. This redshifts distribution confirms that the MILCANN tSZ map enables the detection of high- z galaxy clusters that are not contained in the PSZ2 catalog. From this redshift distribution, we find that new HAD detections are at redshifts ranging from 0.2 to 0.5. Figure 15 also shows the richness distribution for all HAD sources and HAD sources not contained in the PSZ2 that match redmapper galaxy overdensities. We observe that the HAD sources not contained in the PSZ2 catalog are preferentially at lower richness.

5. Multi-wavelength characterization of The HAD sample

In this section we perform a stacking analysis to unveil the average properties of the HAD galaxy cluster candidates. In particular, we focus on the average sub-millimeter SED, on the stacked lensing signal, and on color-color diagnostic using WISE catalog sources.

5.1. Stacked SED of galaxy cluster candidates

For galaxy cluster candidates not seen in PSZ2, we stack the Planck maps per frequency and the IRIS full-sky map at 100 μm (Miville-Deschênes & Lagache 2005). Then, we extract the flux through aperture photometry. Fig. 16, presents the SED we obtained that exhibit both tSZ and IR emissions. Consistently with Planck Collaboration 2015 results XXIII (2015), we model the infra-red emission with a modified black body SED assuming $\beta_d = 1.75$, a dust temperature $T_d = 24$ K, and a mean redshift $\bar{z} = 0.4$. Comparing with previous analysis (Planck Collaboration 2015 results XXIII 2015), the amount of IR emission toward HAD new tSZ detections is compatible with IR emission observed toward PSZ2 confirmed galaxy clusters. We observe that the IR contribution is negligible at 100 and 143 GHz. At 353 and 545 GHz, the IR emission contributes for 25 and 80% of the total signal respectively. At higher frequency, the tSZ contribution is negligible.

5.2. CMB Lensing

We stack the CMB lensing convergence measured by Planck (Planck Collaboration et al. 2015) for all sources from the HAD catalog that are not contained in the PSZ2 galaxy cluster catalog. On Fig. 17 we present the derived stacked signal. We detect an excess in convergence at a 5σ confidence level. Assuming a typical redshift ranging from 0.2 to 0.5 for galaxy clusters, and correcting for purity we compute an average mass of about $2 \cdot 10^{14} M_\odot$ per cluster (see e.g., Melin & Bartlett 2015, for a detailed description of the convergence to mass conversion).

5.3. WISE catalog

We also search for counterpart of the HAD SZ-candidates in the AllWISE full-sky catalog (Cutri et al. 2013). We stack the sources in the AllWISE catalog toward HAD sources that have no PSZ2 counterpart. The stacked density of sources is presented on Fig. 18. We observe a significant AllWISE sources overden-

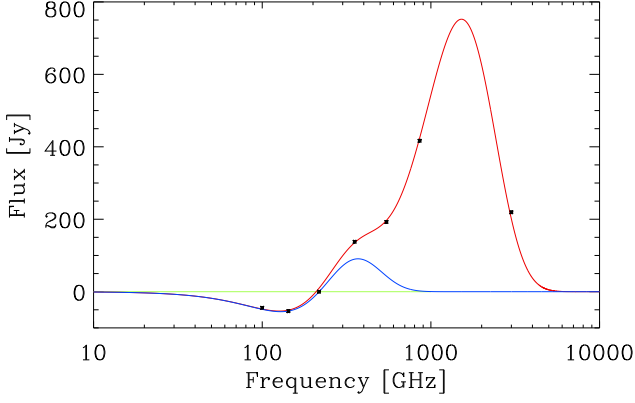


Figure 16. Stacked SED of galaxy-cluster candidates (black sample). The tSZ effect contribution is shown as a solid blue line, and the total SED accounting for tSZ and infra-red emission as a solid red line.

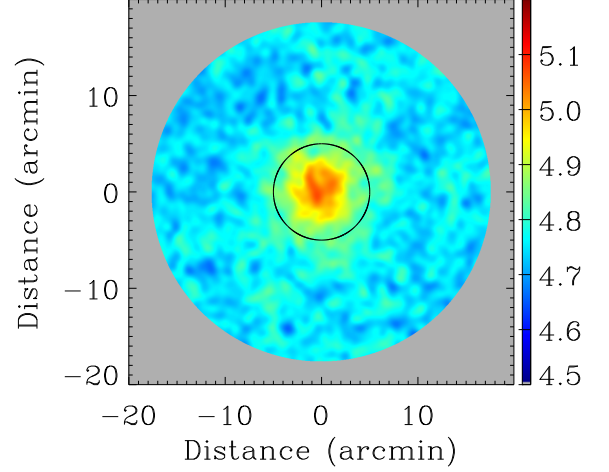


Figure 18. Stacked number of sources in AllWISE catalog toward SZ-candidates not contained in the PSZ2 catalog.

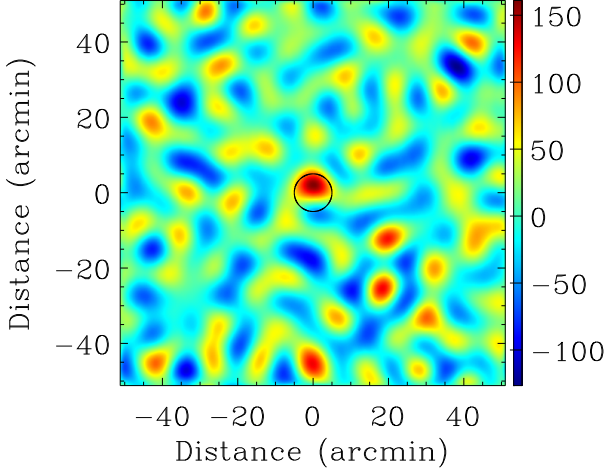


Figure 17. Stacked CMB-lensing convergence map toward HAD SZ-candidates not contained in the PSZ2 catalog.

sity of 23 ± 1^4 per HAD SZ-candidates inside an aperture of 10 arcmin, the background level of the AllWISE sources density map have been estimated between 10 and 15 arcmin.

We also studied the distribution of the AllWISE matching sources in the AllWISE color-color plane. The surface density of HAD-sources member galaxies in the AllWISE catalog is small compared to the total density of all objects. Consequently, we cannot estimate the AllWISE colors for each member galaxies individually and we estimated the color-color distribution of the AllWISE member galaxies.

First we compute the color-color distribution of AllWISE sources inside a radius of 10 arcmin around HAD sources. Then, we compute the same distribution for sources located between 10 and 15 arcmin from the HAD sources. Assuming

⁴ The uncertainty provided is on the average over-density of sources and don't account for intrinsic scatter inside the stacked sample

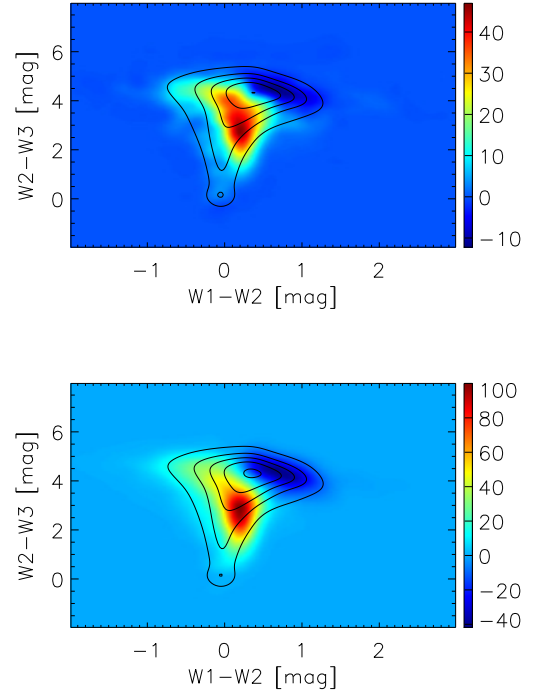


Figure 19. WISE color-color plane for HAD SZ sources not contained (top panels) and contained (bottom panels) in the PSZ2. The color scale shows the distribution for member galaxies, for comparison the distribution for background object is represented by the black contours.

that the background and foreground objects are uniformly distributed on a 15 arcmin scale, we estimate the distribution for member galaxies by computing the sky-area weighted difference between the two distributions.

On Fig. 19, we present the color-color distribution of member

galaxies of HAD sources not in PSZ2 and for those in the PSZ2 catalog. We observe that both populations of tSZ candidates present similar distributions in the (W2-W3)-(W1-W2) color-color plane. These distributions are significantly different from the distribution of background object in the WISE catalog. And present a positive excess for $W1 - W2 \approx 0.2$ and a lack of object for $W2 - W1 \approx 0.8$.

We used the SWIRE galaxy template library (Polletta et al. 2007), and we compute the expected tracks in the WISE color-color plane for 25 galaxy SED templates. When comparing with tracks for various galaxy types, we observe that the negative decrement in the WISE color-color plane is essentially populated by AGNs or high redshift infra-red sources. This implies that tSZ-based catalogs present a selection bias toward galaxy clusters not hosting bright AGN or that present a strong infra-red source in the background. Indeed, for galaxy clusters that host a bright radio-loud AGN the tSZ effect can not be recovered in the microwave and sub-millimeter domain. A similar argument applies when the tSZ effect from a galaxy cluster is contaminated by bright infra-red sources. From these color-color distributions, we can conclude that the galaxy cluster candidates in the HAD catalog are populated by low-redshift ($z < 1$) elliptical, spiral galaxies, and LRG as expected for tSZ samples derived with the Planck experiment.

6. Conclusion

Previous studies performed on galaxy cluster detection with the tSZ effect have shown that a tSZ-map based approach is not optimal and less-efficient than a multi-frequency based approach (Melin et al. 2012). However, we have demonstrated that a tSZ-map combined with a filtering based on an ANN quality assessment enables to construct competitive tSZ source catalogue even with simple detection methods. Our combined approach consists of building an ANN quality assessed tSZ map, MILCANN.

The utilization of the MILCANN full-sky map is tailored for galaxy cluster detection. In particular, the MILCANN tSZ map presents a significantly lower level of noise and foreground residuals than standard tSZ maps. However, the ANN-filtering procedure produces a distortion of the tSZ signal shape and flux. Consequently, the MILCANN map can only be used for galaxy cluster detection purpose and it is not suited for other tSZ analysis such as scaling relations, profiles, or angular power spectrum.

From the MILCANN tSZ map, we have constructed the HAD source catalog that contains 3969 galaxy cluster candidates, with an estimated purity of 90%. This catalog reaches the same purity level than previous galaxy cluster catalog produced from the Planck data (Planck Collaboration 2015 results XXVII 2016) but contains a number of objects 2.5 times larger than the PSZ2 catalog, achieving galaxy clusters detection down to $M_{500} = 10^{14} M_{\odot}$.

We have verified that the number of sources in the HAD catalog is consistent with the expected galaxy cluster abundance derived in the cosmological frame set by the Planck SZ analysis.

Additionally, comparing the HAD catalog with ancillary catalogs, we demonstrated that the HAD galaxy clusters candidates contains new tSZ detections at high redshift and low richness.

Finally we have shown that the sources detected in the MILCANN map present an excess of convergence in CMB lensing maps, compatible with galaxy cluster masses of $2 \cdot 10^{14} M_{\odot}$, and host galaxies with the same spectral behavior than

Planck PSZ2 galaxy cluster member galaxies (elliptical, spiral galaxies, and LRG at $z < 1$).

Acknowledgements. We acknowledge the support of the Agence Nationale de la Recherche through grant ANR-11-BS56-015. We also thank the International space science institute (ISSI) for hosting discussions during the international team meeting "SZ effect in the Planck era".

References

- Abell, G. O., Corwin, Jr., H. G., & Olowin, R. P. 1989, *ApJS*, 70, 1
- Aghanim, N., Hurier, G., Diego, J.-M., et al. 2015, *A&A*, 580, A138
- Arnaud, M., Pratt, G. W., Piffaretti, R., et al. 2010, *A&A*, 517, A92
- Birkinshaw, M. 1999, *Phys. Rep.*, 310, 97
- Bleem, L. E., Stalder, B., de Haan, T., et al. 2014, *ArXiv e-prints*
- Böhlinger, H., Chon, G., & Collins, C. A. 2014, *ArXiv e-prints*
- Böhlinger, H., Schuecker, P., Guzzo, L., et al. 2001, *A&A*, 369, 826
- Bohringer, H., Voges, W., Huchra, J. P., et al. 2000, *VizieR Online Data Catalog*, 212, 90435
- Carlstrom, J. E., Holder, G. P., & Reese, E. D. 2002, *ARA&A*, 40, 643
- Carvalho, P., Rocha, G., & Hobson, M. P. 2009, *MNRAS*, 393, 681
- Cutri, R. M., Wright, E. L., Conrow, T., et al. 2013, *Explanatory Supplement to the AllWISE Data Release Products*, Tech. rep.
- da Silva, A. C., Kay, S. T., Liddle, A. R., & Thomas, P. A. 2004, *MNRAS*, 348, 1401
- Dunkley, J., Hlozek, R., Sievers, J., et al. 2011, *ApJ*, 739, 52
- Ebeling, H., Edge, A. C., Allen, S. W., et al. 2000, *VizieR Online Data Catalog*, 731, 80333
- Ebeling, H., Edge, A. C., & Henry, J. P. 2001, *ApJ*, 553, 668
- Gladders, M. D. & Yee, H. K. C. 2005, *ApJS*, 157, 1
- Hoekstra, H., Mahdavi, A., Babul, A., & Bildfell, C. 2012, *MNRAS*, 427, 1298
- Hurier, G., Hildebrandt, S. R., & Macias-Perez, J. F. 2013, *e-prints* *ArXiv:1007.1149*
- Kay, S. T., Peel, M. W., Short, C. J., et al. 2012, *MNRAS*, 422, 1999
- Koester, B. P., McKay, T. A., Annis, J., et al. 2007, *ApJ*, 660, 239
- Marriage, T. A., Acquaviva, V., Ade, P. A. R., et al. 2011, *ApJ*, 737, 61
- Melin, J.-B., Aghanim, N., Bartelmann, M., et al. 2012, *A&A*, 548, A51
- Melin, J.-B. & Bartlett, J. G. 2015, *A&A*, 578, A21
- Melin, J.-B., Bartlett, J. G., & Delabrouille, J. 2006, *A&A*, 459, 341
- Miville-Deschênes, M.-A. & Lagache, G. 2005, *ApJS*, 157, 302
- Piffaretti, R., Arnaud, M., Pratt, G. W., Pointecouteau, E., & Melin, J.-B. 2011, *A&A*, 534, A109
- Planck Collaboration, Ade, P. A. R., Aghanim, N., et al. 2013, *A&A*, 550, A129
- Planck Collaboration, Ade, P. A. R., Aghanim, N., et al. 2011, *A&A*, 536, A8
- Planck Collaboration, Ade, P. A. R., Aghanim, N., et al. 2015, *ArXiv e-prints*
- Planck Collaboration 2015 results I. 2016, *A&A*, 594, A1
- Planck Collaboration 2015 results XIII. 2015, *ArXiv e-prints*
- Planck Collaboration 2015 results XXII. 2015, *ArXiv e-prints*
- Planck Collaboration 2015 results XXIII. 2015, *ArXiv e-prints*
- Planck Collaboration 2015 results XXVII. 2016, *A&A*, 594, A27
- Planck Collaboration early results. VIII. 2011, *A&A*, 536, A8
- Planck Collaboration results IX. 2014, *A&A*, 571, A9
- Planck Collaboration results. VII. 2014, *A&A*, 571, A7
- Planck Collaboration results. XX. 2014, *A&A*, 571, A20
- Planck Collaboration results. XXI. 2014, *A&A*, 571, A21
- Planck Collaboration results XXVIII. 2014, *A&A*, 571, A28
- Planck Collaboration results XXX. 2014, *A&A*, 571, A30
- Planck Collaboration results XXXII. 2015, *A&A*, 581, A14
- Polletta, M., Tajer, M., Maraschi, L., et al. 2007, *ApJ*, 663, 81
- Reichardt, C. L., Shaw, L., Zahn, O., et al. 2012, *ApJ*, 755, 70
- Rykoff, E. S., Rozo, E., Busha, M. T., et al. 2013, *ArXiv e-prints*
- Sehgal, N., Trac, H., Acquaviva, V., et al. 2011, *ApJ*, 732, 44
- Shirokoff, E., Reichardt, C. L., Shaw, L., et al. 2011, *ApJ*, 736, 61
- Sievers, J. L., Hlozek, R. A., Nolte, M. R., et al. 2013, *J. Cosmology Astropart. Phys.*, 10, 60
- Sifón, C., Menanteau, F., Hasselfield, M., et al. 2013, *ApJ*, 772, 25
- Sunyaev, R. A. & Zeldovich, Y. B. 1969, *Nature*, 223, 721
- Sunyaev, R. A. & Zeldovich, Y. B. 1972, *Comments on Astrophysics and Space Physics*, 4, 173
- The Dark Energy Survey Collaboration. 2005, *ArXiv Astrophysics e-prints*
- van der Burg, R. F. J., Aussel, H., Pratt, G. W., et al. 2016, *A&A*, 587, A23
- Vanderlinde, K., Crawford, T. M., de Haan, T., et al. 2010, *ApJ*, 722, 1180
- Wen, Z. L., Han, J. L., & Liu, F. S. 2012, *ApJS*, 199, 34
- York, D. G., Adelman, J., Anderson, Jr., J. E., et al. 2000, *AJ*, 120, 1579